# Effect of Coulomb breakup on the elastic cross section of the $^{8}$B proton-halo projectile on a heavy, $^{208}$Pb target

J. Rangel,[1] J. Lubian,[1] L. F. Canto,[2,1] and P. R. S. Gomes[1]

[1]*Instituto de Física, Universidade Federal Fluminense, Avenida Litoranea s/n, Gragoatá, Niterói, 24210-340 Rio de Janeiro, Brazil*

[2]*Instituto de Física, Universidade Federal do Rio de Janeiro, CP 68528, 21941-972 Rio de Janeiro, Brazil*

(Received 2 September 2015; revised manuscript received 19 April 2016; published 12 May 2016)

We investigate the role of the breakup channel in the elastic and breakup cross sections, in collisions of proton-halo nuclei. For this purpose, we perform continuum discretized couple channel (CDCC) calculations for the $^{8}$B + $^{208}$Pb system and evaluate polarization potentials. One-channel calculations including the polarization potential are shown to reproduce very well the elastic cross sections obtained by CDCC calculations. We also study the individual contributions of the Coulomb and the nuclear couplings to the cross sections. To complement our study, we compare the effects of the breakup channel in proton-halo and neutron-halo nuclei, performing calculations treating $^{8}$B as a $^{7}$B + $n$ core-nucleon system, with an artificially low breakup threshold. When only the nuclear breakup is considered, this approach can reasonably describe the elastic scattering.

DOI: 10.1103/PhysRevC.93.054610

## I. INTRODUCTION

The scattering and reaction processes involving weakly bound heavy ions, especially halo nuclei, have been a subject of great interest in the last decade [1–5]. Interesting features of the scattering of halo nuclei are similar to those of scattering of highly deformed tightly bound nuclei. The common feature of those very different nuclear systems is the presence of long-range potentials, in addition to the Coulomb potential. In both cases, the coupling interaction extends beyond the radius of the Coulomb barrier. Thus, it excites nonelastic channels even in distant collisions, which leads to small deflection angles.

The general elastic cross section can be written as

$$\frac{d\sigma(\theta)}{d\Omega} = |f_{\rm Ruth}(\theta) + f_{\rm N}(\theta)|^2, \tag{1}$$

where $f_{\rm Ruth}(\theta)$ is the amplitude for Rutherford scattering and $f_{\rm N}(\theta)$ is a correction arising from short-range interactions, such as the nuclear potential and Coulomb and nuclear couplings. Usually, instead of plotting the elastic scattering angular distribution, one plots the ratio of this cross section to the Rutherford cross section, $\sigma/\sigma_{\rm Ruth}$. Then, Eq. (1) leads to the expression

$$\frac{\sigma(\theta)}{\sigma_{\rm Ruth}(\theta)} = 1 + \frac{|f_{\rm N}(\theta)|^2}{|f_{\rm Ruth}(\theta)|^2} + \frac{2\,{\rm Re}\{f_{\rm N}^{*}(\theta) f_{\rm Ruth}(\theta)\}}{|f_{\rm Ruth}(\theta)|^2}. \tag{2}$$

The first two terms on the right-hand side of the above equation come respectively from $f_{\rm Ruth}$ and $f_{\rm N}$, whereas the third gives the interference of the two amplitudes. Note that the Rutherford and the nuclear contributions are positive definite while the interference term is not. It may take positive values (constructive interference) and negative values (destructive interference). Diaz-Torres and Moro [6] have shown that, for loosely-bound nuclei, the Coulomb-nuclear interference around the Coulomb barrier is destructive, owing to the change of the phases of each contribution (nuclear and Coulomb) and to the reduction of their amplitudes in the angular region of the peak of the elastic scattering angular distribution.

In typical collisions at near-barrier energies and forward angles, the Coulomb contribution is dominant [7–9], so that this ratio is essentially equal to 1. This angular region corresponds to distant collisions, where the projectile remains outside the reach of the nuclear forces. As the angle increases, there are oscillations followed by a large bump and a fast decrease. This pattern results from two effects: rainbow scattering, which is associated with the real part of the potential, and Fresnel diffraction, which results from a combination of Coulomb repulsion and strong absorption.

This behavior changes when the collision is strongly affected by long-range coupling potentials, like the dipole or the quadrupole terms of the Coulomb interaction. In such a situation, the usual pattern is modified by the longer range of the imaginary potential. The Fresnel diffraction peak is damped and the ratio $\sigma/\sigma_{\rm Ruth}$ is close to unity only at very forward angles. This effect can be clearly observed in collisions of heavy projectiles with a highly deformed target [10]. In this case, the long-range imaginary potential arises from the Coulomb excitation of rotational states in the projectile.

Other examples of significant suppression of elastic scattering at small angles are the collisions of one- and two-neutron-halo nuclei with heavy targets, such as $^{11}$Be on $^{64}$Zn [11], $^{11}$Be on $^{209}$Bi [12], $^{6}$He on $^{58}$Ni [13], $^{6}$He on $^{208}$Pb [14–16] and $^{6}$He on $^{206}$Pb [17]. This effect is particularly impressive in the data of Cubero *et al.* [18], on the elastic scattering of $^{9,11}$Li projectiles on $^{208}$Pb system. The cross section for the $^{9}$Li projectile exhibited the standard behavior of tightly bound collision partners. However, the cross section for the two-neutron-halo projectile, $^{11}$Li, was drastically suppressed, even at very forward angles and collision energies below the Coulomb barrier. The usual Fresnel peak disappeared completely. A study of the damping effect in collisions of tightly bound and halo projectiles has recently been published [19].

Contrary to neutron-halo projectiles, the elastic scattering of proton-halo projectiles has not been extensively investigated. Important differences between them might exist. In the case of the neutron halo, the Coulomb forces act on the charged fragment but not on the neutron cloud. Thus, the Coulomb

 

polarizability of the projectile tends to be strong, leading to large Coulomb breakup cross section. This effect is expected to be weaker in collisions of proton-halo projectiles, where the Coulomb field of the target acts on the charged core and also on the proton halo.

There are some theoretical studies of collisions of proton-halo projectiles at near-barrier energies. Lubian *et al.* [20] performed continuum discretized coupled channel (CDCC) calculations for $^{8}$B + $^{58}$Ni system. They found that the coupling with continuum states did not lead to appreciable changes in elastic angular distributions. The same system was studied by Tostevin, Nunes, and Thompson [21], who performed CDCC calculations for angular distributions and excitation functions of the $^{7}$Be fragment, produced by the breakup process. Lubian *et al.* [22] investigated the effect of breakup on the fusion and quasielastic cross sections for the same system. The relative importance of Coulomb and nuclear breakups on the elastic and total breakup cross section for this system was investigated in Refs. [20,23]. The authors concluded that both the Coulomb and the nuclear contributions to the breakup cross section are important, and that there was strongly destructive Coulomb-nuclear interference.

The present work reports results of CDCC calculations for collisions of the same proton-halo projectile, but on $^{208}$Pb, which is much heavier than the target considered in previous works. Owing to the strong Coulomb field of the target and the low breakup threshold of $^{8}$B, 0.137 MeV, Coulomb breakup is expected to play a very important role. We evaluate $^{8}$B breakup angular distributions and the influence of the breakup process on elastic scattering. We perform calculations of cross sections at energies above and below the Coulomb barrier, which is at 50 MeV (or 52 MeV in the laboratory frame). There are no experimental data for this system at near-barrier energies. However, Yang *et al.* [24] measured the elastic scattering angular distribution for $^{8}$B + $^{\text{nat}}$Pb at a higher energy (around three times the Coulomb barrier). In that work they observed a Fresnel pattern in the elastic scattering angular distribution and negligible effect (within the error bars) of the coupling to continuum states from the CDCC calculation.

This paper is organized as follows. In Sec. II we describe the main features of the CDCC method applied to the $^{8}$B + $^{208}$Pb system. We discuss the optical potentials used in our calculations and the evaluation of the contributions from the Coulomb and the nuclear couplings to the breakup cross sections. In Sec. III we show results of our calculations for elastic scattering, breakup, and polarization potentials. These potentials are devised to simulate channel coupling effects in single channel calculations. In Sec. IV we discuss the difference between cross sections for proton-halo and neutron-halo projectiles. Finally, in Sec. V we present a summary and the conclusions of our work.

## II. CDCC CALCULATIONS FOR THE $^{8}$B + $^{208}$Pb SYSTEM

We have performed three-body CDCC calculations to describe collisions of $^{8}$B projectiles with a $^{208}$Pb target. In our calculations, we adopted the same model space of Refs. [25,26] and used the FRESCO computer code [27]. Calculations along these lines were able to describe the elastic scattering and the breakup of $^{8}$B projectiles in collisions with a $^{58}$Ni target [20,21], as well as the energy distribution of the $p$ and $^{7}$Be fragments [21] produced in the breakup process. They were also able to describe the elastic scattering of the same projectile on a $^{12}$C target [28].

Since the details of the model space are available in Refs. [25,26], we give just a brief description here. The $^{8}$B projectile can be modeled as a $^{7}$Be + $p$ system. In its ground state, the proton moves around the $^{7}$Be core in a $1p_{3/2}$ orbital. The remaining projectile states included in the model space are in the continuum. They are then approximated by a finite set of square-integrable wave functions given by energy averages of $^{7}$Be + $p$ scattering states within a given energy range. These *bin states* are labeled by the midpoint of the energy interval and by its angular momentum. We consider orbital angular momenta up to $l = 5\hbar$. Using the bin states, one builds an orthonormal basis to describe the continuum space of the projectile. The details of this procedure can by found in Refs. [29,30]. All intrinsic states of the projectile (bound and unbound) used in our calculations were determined by solving the Schrödinger equation for the $^{7}$Be-$p$ system, with the potential of Ref. [31]. Thus, there is no free parameter.

The angular momentum projected three-body wave functions are then written as linear combinations of products of the intrinsic projectile's wave function and the wave function of the projectile-target relative motion, coupled to total angular momentum $J$ and projection $M$. That is,

$$\Psi^{JM}(\mathbf{R},\mathbf{r}) = \sum_{\alpha} \frac{f_{\alpha,J}(R)}{R}\, \mathcal{Y}_{\alpha}^{JM}(\hat{\mathbf{R}},\mathbf{r}), \tag{3}$$

where $\mathbf{r}$ is the internal coordinate of the projectile and $\mathbf{R}$ is the projectile-target relative coordinate. In Eq. (3) $\mathcal{Y}_{\alpha}^{JM}(\hat{\mathbf{R}},\mathbf{r})$ represents the tensor product of the angular part of the projectile-target relative wave function with the intrinsic wave function of the projectile. It is important to note that the internal structure of the target was not considered in the coupled equations. This is justified by the fact that the cross sections for excitations of the doubly-magic $^{208}$Pb target are low [24]. However, the influence of target excitations on elastic scattering and breakup reactions can be taken into account adopting imaginary potentials with longer ranges. This point will be discussed in the next sub-section.

Inserting Eq. (3) into the Schrödinger equation and carrying out some algebra, one obtains the set of coupled equations

$$[H_{\alpha} - (E - \varepsilon_{\alpha})] f_{\alpha,J}(R) + \sum_{\alpha' \neq \alpha} i^{\mathrm{L}'-\mathrm{L}}\, V_{\alpha\alpha'}(R)\, f_{\alpha',J}(R) = 0, \tag{4}$$

where

$$H_{\alpha} = -\frac{\hbar^2}{2\mu}\left[\frac{d^2}{dR^2} - \frac{L(L+1)}{R^2}\right] + V_{\alpha\alpha}(R) \tag{5}$$

is the Hamiltonian in channel $\alpha$, and $\varepsilon_{\alpha}$ is the intrinsic energy of the projectile in this channel. In the present calculation, $\alpha_0 = 0$ stands for the elastic channel, where the projectile is in its ground state ($\varepsilon_0 = 0, l_0 = 1, j_0 = \frac{3}{2}$), and $\alpha \neq 0$ corresponds to a projectile's state in the continuum, in the bin state with by $\varepsilon_{\alpha}$.

The projectile-target interaction is given by the sum

$$V(\mathbf{R},\mathbf{r}) = V_{p\text{-T}}(\mathbf{r}_v) + V_{^7\text{Be-T}}(\mathbf{r}_c), \quad (6)$$

where T stands for the target, $V_{p\text{-T}}$ and $V_{^7\text{Be-T}}$ are the optical potentials responsible for the elastic scattering of the valence particle ($p$) and the core ($^7$Be) from the target ($^{208}$Pb). They are functions of the position vectors of the valence particle ($\mathbf{r}_\text{v}$) and the core ($\mathbf{r}_\text{c}$), respectively. These vectors are given in terms of the vector joining the centers of the collision partners ($\mathbf{R}$) and the vector between the valence particle and the core ($\mathbf{r}$), by the standard relations

$$\mathbf{r}_\text{v} = \mathbf{R} + \frac{A_\text{c}}{A_\text{P}}\,\mathbf{r} \quad \text{and} \quad \mathbf{r}_\text{c} = \mathbf{R} - \frac{A_\text{v}}{A_\text{P}}\,\mathbf{r}, \quad (7)$$

where $A_\text{c}$, $A_\text{v}$, and $A_\text{P}$ are the mass numbers of the core, the valence particle, and the projectile, respectively.

The matrix elements of Eq. (4) are given by

$$V_{\alpha\alpha'}(R) = \langle \phi_\alpha(\mathbf{r}) | V(\mathbf{R},\mathbf{r}) | \phi_{\alpha'}(\mathbf{r}) \rangle, \quad (8)$$

where $\phi_\alpha(\mathbf{r})$ stands for both the bound states of the projectile and the bin wave functions.

To solve the set of coupled equations [Eq. (4)], the matrix elements $V_{\alpha\alpha'}(R)$ are expanded in multipoles up to $\lambda = 4$, and their multipole components are evaluated by numerical integration over a mesh of radial distances (between the core and the valence particle) distributed bewteen $r = 0$ and $r_\text{max} = 80$ fm. The coupled equations are then solved numerically considering projectile-target distances up to $R = 500$ fm and angular momenta up to $1000\hbar$.

### A. The real and imaginary parts of the fragment-target potentials

For the real parts of $V_{p\text{-T}}$ and $V_{^7\text{Be-T}}$, we adopt the Akyüz-Winther potential [32], which is a common practice in heavy ion scattering.

The choice of the imaginary parts of $V_{p\text{-T}}$ and $V_{^7\text{Be-T}}$ requires some discussion. Clearly, they must account for the fusion of the fragments with the target. If fusion is the only relevant nonelastic process affecting the cross section, the imaginary potentials should produce strong absorption and have a short range. In this case, we parametrize them by Woods-Saxon functions, with depth $W_0 = -50$ MeV, radius $R_0 = 1.06\,(A_i^{1/3} + 208^{1/3})$ fm, were $i$ stands either for the $^7$Be core or for the proton, and diffusivity $a = 0.2$ fm.

On the other hand, if the imaginary potentials are also associated with direct reactions, such as excitations of $^{208}$Pb, they must have a longer range, in order to produce absorption in peripheral collisions. In this case we assume that they have the same shape as the real potentials but have a slightly lower intensity. We use the relations

$$\text{Im}\{V_{^7\text{Be}-\text{T}}(\mathbf{r}_\text{c})\} = 0.78\,\text{Re}\{V_{^7\text{Be}-\text{T}}(\mathbf{r}_\text{c})\}, \quad (9)$$

$$\text{Im}\{V_{\text{p}-\text{T}}(\mathbf{r}_\text{v})\} = 0.78\,\text{Re}\{V_{\text{p}-\text{T}}(\mathbf{r}_\text{v})\}. \quad (10)$$

This procedure has been successfully used in many situations [33] where the nuclear interactions are modeled by the São Paulo potential [34,35], which is similar to the Akyüz-Winther potential at near-barrier energies.

When one uses long-range imaginary potentials, the current diverted into channels associated with target excitation is completely excluded from the coupled equation. Thus, it does not contribute to any channel included in the coupled equations. This is consistent with measurements of elastic scattering or elastic breakup, where events in which the target is left in an excited state are discarded. Therefore, long-range imaginary potentials is the appropriate choice for calculations of elastic scattering and elastic breakup.

The situation is different in calculations of noncapture breakup (NCBU) or total fusion (TF). In measurements of these quantities the events are registered independently of the intrinsic state of the target. Thus, the influence of channels with target excitation cannot be mocked up by long-range absorption. Clearly, the couplings of the continuum with the elastic channel are not the same as those of the continuum with channels where the target is excited. However, ignoring this difference might be better than neglecting transitions from inelastic channels to the continuum altogether. A similar argument can be given in the case of total fusion.

In view of the above discussion, we will adopt the following procedure: (*i*) calculations of elastic scattering and polarization potentials will be performed with long-range imaginary potentials and (*ii*) calculations of breakup will be performed with both long-range and short-range imaginary potentials.

### B. Coulomb breakup, nuclear breakup, and Coulomb-nuclear interference

Now we investigate the roles of the Coulomb and the nuclear couplings in the breakup process. For this purpose we perform independent calculations considering only the Coulomb or the nuclear part of the coupling interaction. That is, in each case we perform a CDCC calculation neglecting all off-diagonal matrix elements of either the nuclear or the Coulomb part of the potential. This procedure is described in further detail below.

First, we write the full projectile-target interaction of Eq. (6) as

$$V(\mathbf{R},\mathbf{r}) = V_\text{opt}(\mathbf{R},\mathbf{r}) + \Delta V(\mathbf{R},\mathbf{r}), \quad (11)$$

where $V_\text{opt}(\mathbf{R},\mathbf{r})$ and $\Delta V(\mathbf{R},\mathbf{r})$ are respectively the diagonal and the off-diagonal parts of the interaction in channel space. They are given by the spectral representations

$$V_\text{opt} = \sum_i |\phi_i)\,(\phi_i|V|\phi_i)\,(\phi_i| \quad (12)$$

and

$$\Delta V = \sum_{i\neq j} |\phi_i)\,(\phi_i|V|\phi_j)\,(\phi_j|, \quad (13)$$

where $\phi_i$ and $\phi_j$ represent both the bound eigenfunctions of the projectile and its unbound eigenfunctions, within the continuum discretized approximation. Note that $V_\text{opt}$ plays the role of an optical potential whereas $\Delta V$ is the channel coupling part of the interaction.

Next, we split the coupling interaction into its Coulomb and nuclear components,

$$\Delta V = \Delta V^{(C)} + \Delta V^{(N)}. \tag{14}$$

This can be done separating the Coulomb and the nuclear parts of the $V_{^7\text{Be-T}}$ and $V_{p\text{-T}}$ potentials of Eq. (6), and then using Eq. (13) for the Coulomb and for the nuclear components individually.

To assess the importance of the Coulomb couplings, we drop $\Delta V^{(N)}$ and solve the CDCC equations for the interaction $V_{\text{opt}} + \Delta V^{(C)}$. We then get the scattering amplitudes $f^{(C)}_{\alpha,0}(\theta)$. The breakup cross section is then evaluated by the expression

$$\frac{d\sigma^{(C)}_{\text{bu}}(\theta)}{d\Omega} = \sum_{\alpha\neq 0} \frac{k_\alpha}{k_0} \left| f^{(C)}_{\alpha,0}(\theta) \right|^2. \tag{15}$$

Next, we solve the CDCC equations keeping the nuclear part of the coupling but dropping $\Delta V^{(C)}$. That is, we solve the coupled equations for the interaction $V_{\text{opt}} + \Delta V^{(N)}$. In this way, we get the scattering amplitudes $f^{(N)}_{\alpha,0}(\theta)$ and the corresponding breakup cross section $d\sigma^{(N)}_{\text{bu}}(\theta)/d\Omega$.

The above procedure has the advantage of being very easy to implement. However, it has a shortcoming. The amplitudes $f^{(C)}_{\alpha,0}(\theta)$ and $f^{(N)}_{\alpha,0}(\theta)$ are not associated with the same scattering wave function. They are solutions of scattering problems with different interactions. Therefore, the Coulomb-nuclear interference term cannot be evaluated directly.

## III. RESULTS AND DISCUSSION

### A. Elastic scattering

We begin with the elastic scattering of $^8$B projectiles on $^{208}$Pb, at the bombarding energy $E_{\text{lab}} = 170.3$ MeV. The results of our CDCC calculations are represented by a solid line in Fig. 1, in comparison with the data of Ref. [24]. The dashed line corresponds to results of a one-channel calculation, which neglects off-diagonal matrix elements of the interaction ($\Delta V = 0$). Clearly, the CDCC calculation reproduces the data very well. An equally good agreement between theory and experiment was reached in a similar calculation using a different optical potential [24]. The predictions of the one-channel calculations are poorer. The Fresnel peak is shifted to a slightly lower angle, and the cross sections at higher angles are underestimated.

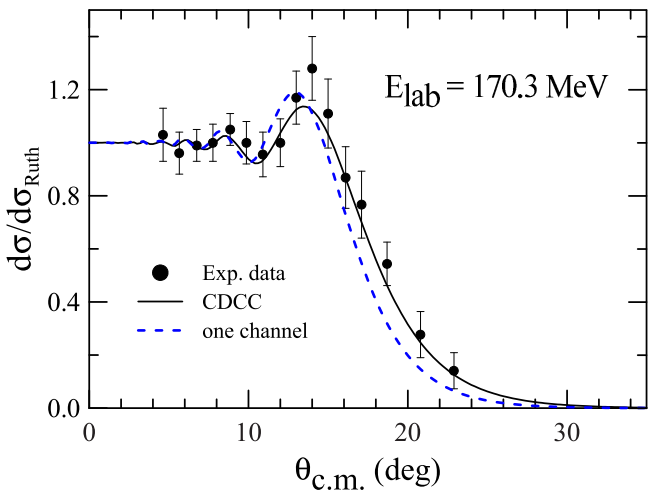


FIG. 1. Elastic scattering of $^8$B on $^{208}$Pb at 170.3 MeV. The solid line and the dashed line correspond, respectively, to CDCC calculations taking into account all couplings and to a one-channel calculation with all couplings switched off. The data are from Ref. [24].

After this preliminary application, we carry out a detailed investigation of the influence of the breakup process on elastic scattering. First, we study the importance of the multipole components of the coupling, performing several calculations.

The results are shown in Fig. 2. The thin solid lines correspond to one-channel calculations, where all couplings are switched off. The remaining curves are results of CDCC calculations, where the multipoles expansion of the coupling

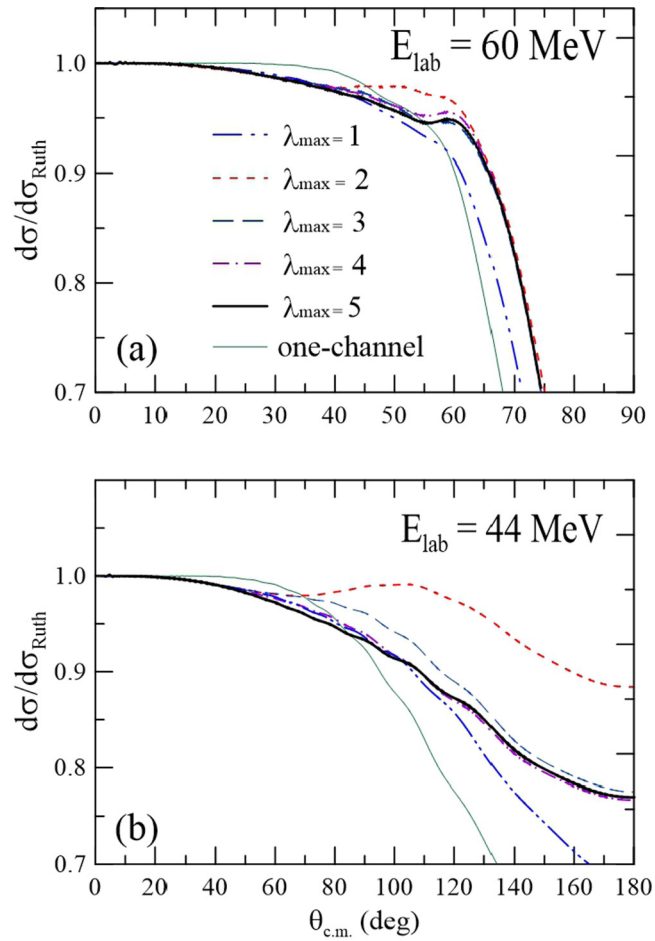


FIG. 2. Elastic angular distributions for different cutoff values in the multipole expansion of the interaction, $\lambda_{\text{max}}$. The curves correspond to results of the CDCC calculations for $\lambda_{\text{max}} = 1$, 2, 3, 4, and 5. The one-channel calculations (thin solid lines) consider only the expectation value of the interaction, calculated for the elastic channel. To enhance the differences among the lines, we restrict the $y$ axis to values between 0.7 and 1.0. For the same reason, we use different angular regions for $E_{\text{lab}} = 60$ MeV (a) and $E_{\text{lab}} = 44$ MeV (b) in the $x$ axis. Further details can be found in the text.

interaction is truncated at the different $\lambda_{max}$ indicated in the legend. We show results for two bombarding energies. In the bottom panel the bombarding energy is 44 MeV (8 MeV below the barrier) and in the top panel the energy is 60 MeV (8 MeV above the barrier). We have performed calculations at other near-barrier energies. They lead to similar results, which are not worth reporting here.

Clearly, the calculations converge at $\lambda_{max} = 4$. The curves for $\lambda_{max} = 4$ and $\lambda_{max} = 5$ can hardly be distinguished, at both bombarding energies. We then truncate the multipole expansions at $\lambda_{max} = 4$ in CDCC calculations of this work. Comparing the converged CDCC cross sections with those of one-channel calculations, one concludes that, at both bombarding energies, the net effect of the breakup coupling is to dampen the cross sections at forward angles and to enhance them at larger angles. The ratio between the CDCC and the Rutherford cross sections is less than 1, even at angles as small as $\theta \sim 40^\circ$. This is due to the long range of the Coulomb dipole coupling. Thus, it is a purely dynamic effect. We recall that all static effects of the $^8$B halo are already included in the single channel calculation. The reason is that the optical potential acting on the elastic channel is the expectation value of the interaction [Eq. (6) for $\alpha = \alpha' = 0$] taken with respect to the ground state of $^8$B, which takes the halo into account.

We have also checked the stability of the results with respect to the details of the continuum discretization. We got good convergence using bins of width $\Delta\varepsilon = 2$ MeV, but the cutoff values of the energy and the orbital angular momentum depended on the bombarding energy. At $E_{lab} = 44$ MeV, $\varepsilon_{max} = 8$ MeV and $l_{max} = 4$ were enough to guarantee convergence, whereas at $E_{lab} = 60$ MeV it was necessary to increase the cutoff values to $\varepsilon_{max} = 12$ MeV and $l_{max} = 5$.

Now we study the influence of the Coulomb and the nuclear breakup couplings on elastic scattering. Investigations of this kind have been carried out for the lighter $^8$B + $^{58}$Ni system at near-barrier energies [20,23]. They lead to the conclusions that the contributions from the two couplings are of the same order, and that they interfere destructively. In the case of the $^8$B + $^{208}$Pb system, where the target has a larger charge, one could expect that the importance of the Coulomb couplings is increased. On the other hand, one cannot predict the behavior of the Coulomb-nuclear interference.

Figure 3 shows elastic angular distributions of CDCC calculations with full channel couplings (thick solid lines), with pure Coulomb couplings (dotted lines), and pure nuclear couplings (dashed lines). As we explained in the previous section, the diagonal part of the full interaction, $V_{opt}$, is kept in all calculations. For comparison, we show also the results of one-channel calculations (thin solid lines). As in the previous figure, the calculations were performed at $E_{lab} = 60$ [panel (a)] and 44 MeV [panel (b)].

Comparing the dashed and dotted lines with the thin solid line, one sees that the nuclear and the Coulomb couplings produce opposite effects. The nuclear couplings (dashed lines) enhance the elastic cross sections whereas the Coulomb couplings (dotted lines) suppress them. At 44 MeV, one observes that the effects of the Coulomb couplings are noticeable at angles as low 30°, while those of the nuclear couplings start only at $\theta \sim 60^\circ$. This is due to the long

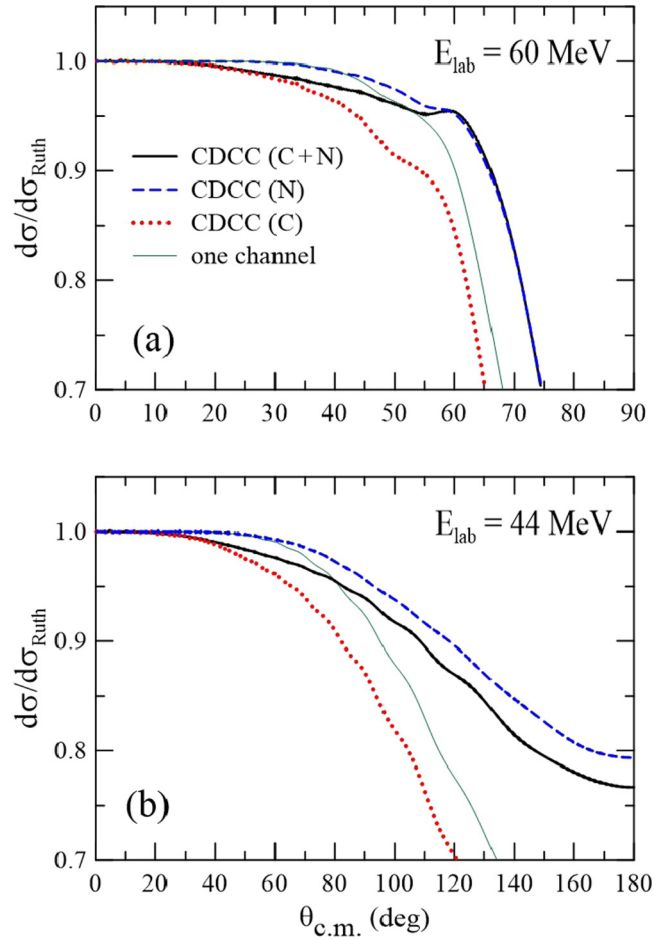


FIG. 3. Influence of Coulomb and nuclear couplings on elastic angular distributions. The figure shows results of one-channel calculations (thin solid lines) and of CDCC calculations with different couplings. The thick solid lines take into account all couplings, and the dashed and the dotted lines are restricted to nuclear and to Coulomb couplings, respectively.

range of the Coulomb dipole coupling, which reaches distant collisions associated with small scattering angles. The angular distributions at 60 MeV show a similar behavior but the effects of the couplings can be observed at slightly smaller scattering angles. Comparisons between the thick and the thin solid lines indicate that the net effect of the Coulomb + nuclear couplings is to reduce the one-channel cross sections at small angles and to enhance them at large angles. The transition between the two behaviors takes place at $\theta \sim 90^\circ$, for $E_{lab} = 44$ MeV, and at $\theta \sim 50^\circ$, for $E_{lab} = 60$ MeV.

Comparing the three CDCC calculations one sees that the curves associated with full couplings fall between the curves associated with pure nuclear and pure Coulomb couplings. This indicates that there is destructive Coulomb-nuclear interference in the elastic angular distributions. A similar situation was encountered for the $^8$B + $^{58}$Ni [20,23], $^{11}$Be + $^{64}$Zn [6], and $^6$He + $^{208}$Pb [6] systems, among others.

Finally, we study the influence of the breakup threshold on the elastic angular distribution. For simplicity, we restrict the discussion to the energy above the barrier, $E_{lab} = 60$ MeV.

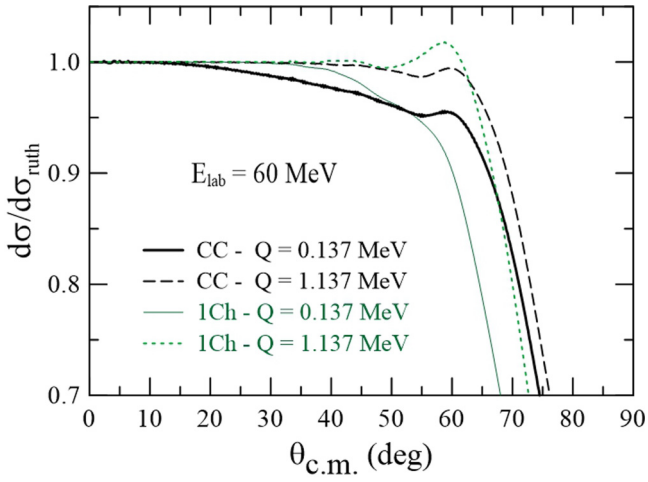


FIG. 4. Influence of the breakup threshold ($Q$) of $^8$B on the elastic angular distribution. See the text for details.

We perform a CDCC calculation with full couplings for the artificially large value of the breakup threshold, $Q = 1.137$ MeV. That is, we increase the breakup threshold by 1 MeV. An increase in the separation energy of the proton reduces absorption in two ways. First, it weakens the strength of the breakup couplings, leading to less breakup absorption. Second, it reduces the range of the ground state wave function of the projectile, $\phi_0$. Consequently, the range of the optical potential, which is given by the expectation value of the interaction for $\phi_0$ [see Eq. (12)], is reduced. In this way, the imaginary potential associated with inelastic channels is also reduced.

Figure 4 shows the results of CDCC calculations (with Coulomb + nuclear couplings) for $Q = 1.137$ MeV (thick dashed line) and for the actual $Q$ value, 0.137 MeV (thick solid line). For comparison, the results of the corresponding one-channels calculations are also shown (thin dotted and solid lines, respectively). First, one observes that the increase of the $Q$ value reduces the influence of the breakup channel in the CDCC calculations, making the angular distribution closer to the Fresnel pattern, commonly observed in heavy-ion scattering. The ratio to the Rutherford cross section remains close to one up to $\sim 60^\circ$, and the rainbow maximum is enhanced. This behavior is still more noticeable in the one-channel calculation with the large $Q$ value, where the rainbow maximum is more pronounced. This is not surprising, since there is no Coulomb breakup in the one-channel calculation. In this way, the maximum is not damped by the long-range absorption associated with Coulomb breakup. We conclude that the CDCC cross section has a significant dependence on the breakup threshold. The increase of 1 MeV in this threshold leads to appreciable changes in the cross section, mainly at intermediate angles where the ratio to the Rutherford cross section begins to fall.

### B. The breakup cross section

In this section we study the contributions from the Coulomb and nuclear couplings to the breakup cross section. Now we should distinguish elastic breakup from NCBU. In the former, the target must remain in its ground state, whereas in the latter the final state of the target is irrelevant. To be consistent with the experimental situation, in the calculations of elastic breakup the imaginary part of the fragment-target potentials should have a long range. In this way, the absorption in grazing collisions takes into account the loss of inelastic events that are discarded in the measurements. Regarding NCBU, the situation is not clear. The problem is that the channels where the target is excited also contribute to the breakup process. In this case, it is better to keep the contributions from peripheral collisions and for this purpose the imaginary potentials should be of short range.

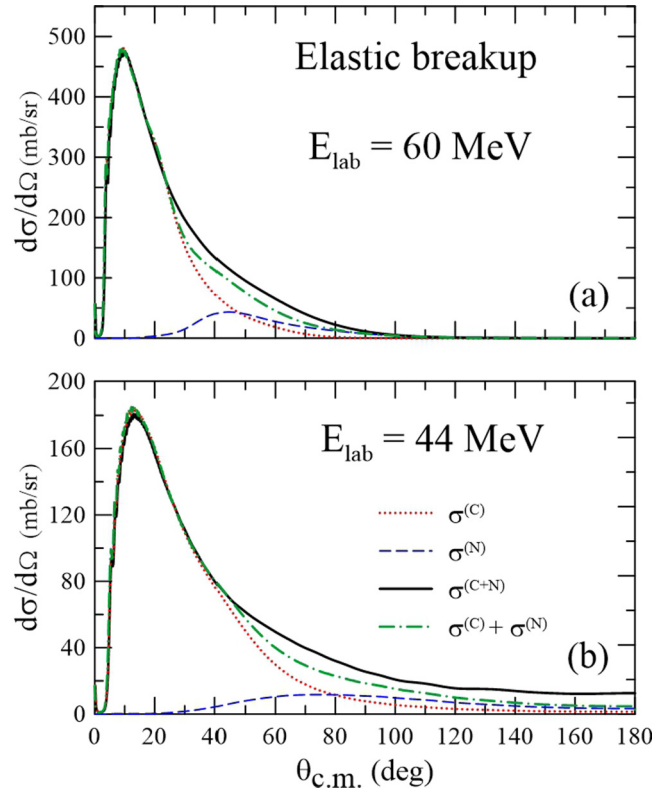


FIG. 5. Contributions from the Coulomb and the nuclear couplings to the breakup cross sections at energies around the Coulomb barrier. For details see the text.

In Fig. 5 we compare different CDCC calculations of elastic breakup. The dotted lines, the dashed lines and the solid lines correspond respectively to the breakup cross sections resulting from Coulomb couplings, from nuclear couplings, from the full coupling interaction. We show also the sum of breakup cross sections obtained with pure Coulomb and pure nuclear couplings (dot-dashed lines). The bombarding energies are the same as in the previous figure: $E_{\rm lab} = 44$ and 60 MeV. Clearly, the breakup cross sections at forward angles is completely dominated by the Coulomb couplings. This is a trivial consequence of the long-range of the Coulomb dipole term. Forward angles correspond to trajectories with large impact parameters, which remain outside the reach of the nuclear couplings. Then, at intermediate angles the two couplings lead to contributions of the same order whereas nuclear breakup is larger than Coulomb breakup at backward

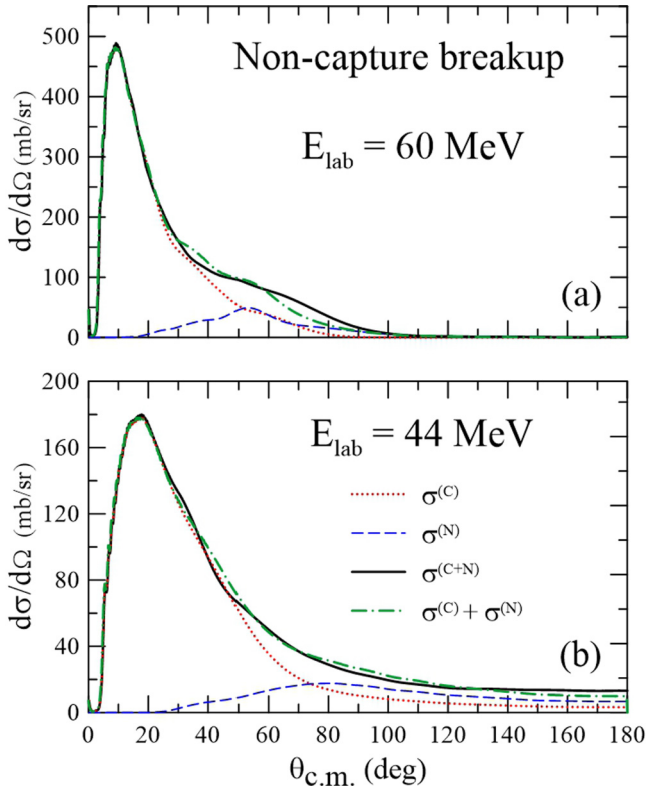


FIG. 6. Contributions from the Coulomb and the nuclear couplings to the breakup cross sections at energies around the Coulomb barrier. For details see the text.

angle. The cross sections for $^{8}$B breakup in collisions with a $^{58}$Ni target were qualitatively similar [20]. The Coulomb-nuclear interference in the breakup cross section is estimated as the difference between the solid and the dot-dashed lines. This indicates that the interference is constructive. A different conclusion was reached in the case of elastic scattering, where the interference is destructive (see Fig. 3).

We remark that the interference patterns in the breakup and in the elastic cross sections are not directly related. The breakup $T$ matrix can be written as the sum of the matrix elements associated with the couplings $\Delta V^{(C)}$ and $\Delta V^{(N)}$ [see Eqs. (13) and (14)]. Thus, the interference pattern results from the relative phase of these two matrix elements. On the other hand, the elastic $T$ matrix has contributions from the Coulomb and the nuclear couplings, but it contains also a contribution from potential scattering, represented by the matrix element of the optical potential of Eq. (12). In this case the interference pattern is more complicated, as it depends on relative phases of three amplitudes. Therefore, the interference patterns of the two cross sections do not have to be similar.

In Fig. 6 we show a similar plot but now the calculations have been performed with short-range imaginary potentials. In this case, the results correspond to NCBU. The notation of the curves is the same as in the previous figure. One notices that the cross sections for Coulomb breakup are very similar to the ones of the previous figure. This is not surprising, as the reduction of the imaginary potentials is not expected to affect the distant collisions that give the main contribution to Coulomb breakup. On the other hand, the shorter range of the imaginary potentials slightly increases the nuclear breakup cross section, specially at the sub-barrier energy of 44 MeV. Comparing the solid and the dot-dashed lines, one concludes that the Coulomb-nuclear interference is constructive, but it is weaker than in the case of elastic breakup.

### C. Polarization potentials

The concept of polarization potentials is widely used in nuclear reaction theory. This potential, denoted by $V_{\rm pol}$, is used in the one-channel description of elastic scattering, and it is defined by the condition that it leads to the same wave function as that obtained from the coupled channel equations. That is, adding $V_{\rm pol}$ to the elastic Hamiltonian, given by Eq. (5) for $\alpha = 0$, the elastic wave function must satisfy the equation

$$[H_0 + V_{\rm pol}(R) - E] f_{0,J}(R) = 0. \tag{16}$$

Since in our energy scale $\varepsilon_0 = 0$, the relative energy in the elastic channel is equal to the total energy. Comparing the above equation with Eq. (4), one immediately gets the exact expression for the polarization potential:

$$V^{(J)}_{\rm pol}(R) = \frac{1}{f_{0,J}(R)} \sum_{\alpha\neq 0} i^{L_\alpha - L_0}\, V_{0\alpha}(R)\, f_{\alpha,J}(R), \tag{17}$$

where $J$ is the total angular momentum and $L_0$ and $L_\alpha$ are respectively the orbital angular momenta of the projectile-target motion in the elastic channel and in channel $\alpha$. Since this potential clearly depends on angular momentum, we added the value of $J$ as a superscript.

However, the definition of Eq. (17) has some shortcomings. First, it leads to poles at the zeros of the wave function appearing in the denominator. Second, this potential has an undesirable dependence on $J$. These difficulties are avoided in the approximate polarization potential of Thompson *et al.* [36]. They proposed the expression

$$V_{\rm pol}(R) = \frac{\sum_J \omega_J(R)\, V^{(J)}_{\rm pol}(R)}{\sum_J \omega_J(R)}, \tag{18}$$

where

$$\omega_J(R) = (2J+1)[1 - |S_{0,J}|^2] f_{0,J}(R). \tag{19}$$

Above, $S_{0,J}$ is the elastic $S$ matrix at the angular momentum $J$.

The potential of Eq. (18) is an average of $J$-dependent polarization potentials, with the weight function $\omega_J(R)$. The method of Thompson *et al.* has been successfully used by many authors to evaluate polarization potentials associated couplings with the breakup channel [26,37–39].

We evaluated the polarization potentials associated with breakup couplings in $^{8}$B -$^{208}$Pb scattering, at $E_{\rm lab} = 60$ MeV. The real and imaginary parts of the potentials are plotted in panels (a) and (b) of Fig. 7, respectively. The figure shows the polarization potential in the barrier region ($R_{\rm B} \sim 11$ fm) and outside the barrier. We used long-range absorption in the $V_{p\text{-T}}$ and $V_{^7\text{Be-T}}$ interactions, which is appropriate for calculations of elastic scattering.

Inspecting panel (a), one concludes that the real part of the polarization potential is appreciable, being repulsive at long distances and oscillating near the barrier radius.

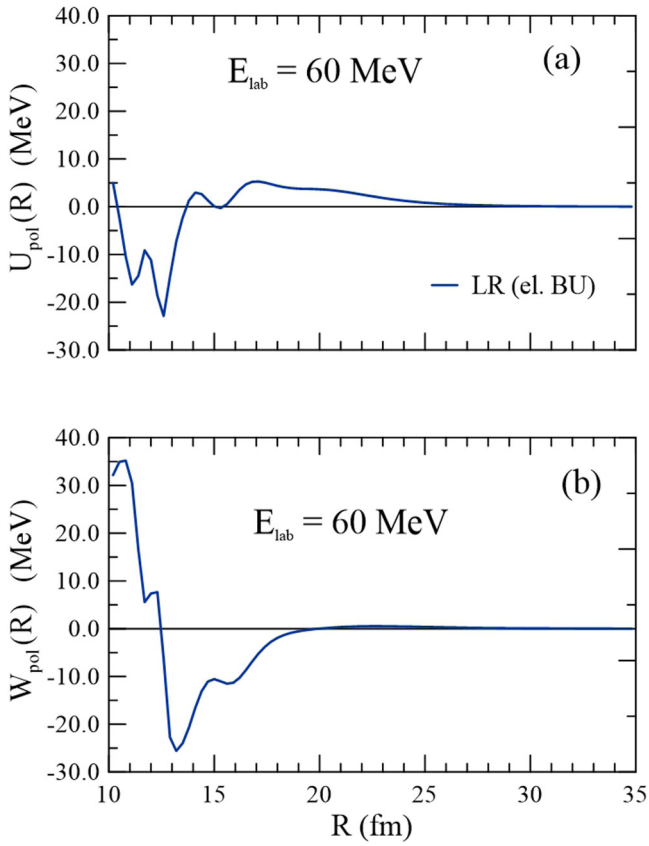


FIG. 7. Real (a) and imaginary (b) parts of the breakup polarization potentials for the $^{8}B + ^{208}Pb$ system. The polarization potential was obtained with long-range absorption. See the text for details.

The imaginary part of the polarization potential is shown in panel (b). It is strongly absorptive at long separations, reaching $-20$ MeV at $R \sim 14$ fm. This behavior is responsible for the damping of the elastic cross section at forward angles observed in panel (a) of Fig. 2. On the other hand, the imaginary potential takes positive values in the neighborhood of the Coulomb barrier. At first, it may look strange that the polarization potential acts as a source of flux in this region. However, this is not unusual in approximate polarization potentials. This behavior is acceptable, provided that the net effect of the potential is absorption of flux.

Since the polarization potential of Thompson *et al.* is approximated by an average of exact polarization potentials for different angular momenta, one should make sure that it gives a reasonable description of the collision. We checked this point by evaluating the elastic angular distribution at $E_{lab} = 60$ MeV given by the solution of the one-channel equation with the potential $V_{00} + V_{pol}$ (dashed line), and comparing it with the CDCC angular distribution (solid line). The results are shown in Fig. 8. We conclude that the one-channel calculation including the polarization potential reproduces the CDCC cross section very well. At forward angles, where the ratio to the Rutherford cross section begins to deviate from 1 (indicated by the dotted line), the solid and the dashed lines are nearly identical. At larger angles, there is some difference but it is very small.

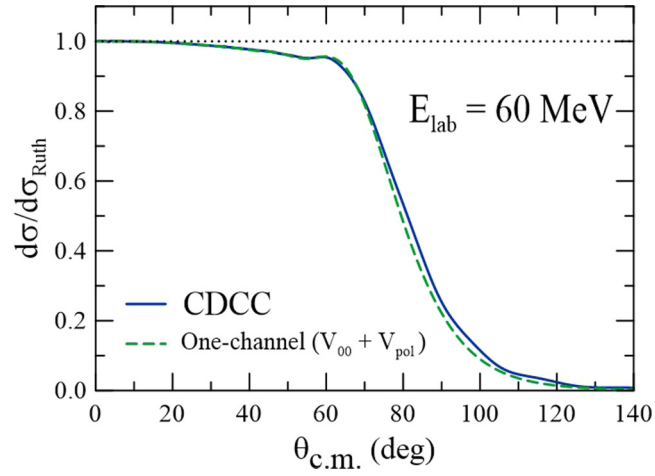


FIG. 8. Comparison of the elastic cross section of the CDCC calculation (solid line) and the cross section obtained with a one-channel calculation including the polarization potential (dashed line).

To close this section, we discuss the use of the polarization potentials considered above. One should have in mind that the polarization potential of Thompson *et al.* [36] is not meant as an alternative to the calculation of cross sections. Its determination requires the knowledge of the wave functions and if they are known, the cross sections are readily available. However, they have other uses. First, they provide a potential scattering description of otherwise complicated channel coupling effects. Second, they are very useful to simplify the description of collisions in which different kinds of channel coupling effects are relevant. For example, when one tries to describe collisions of a weakly bound projectile, say $^{11}$Li, with a highly deformed target, say $^{154}$Sm, the breakup channel as well as rotational channels of the target are of utmost importance. However, performing the appropriate CDCC calculation with the inclusion of target excitation would be prohibitively complicated. In this case, one can perform a coupled channel calculation involving the rotational channels using a breakup polarization potential. Clearly, one should use the polarization potential with short-range fragment-target absorption. Otherwise, there would be double counting of the effects of inelastic excitations of the target.

## IV. PROTON HALO VERSUS NEUTRON HALO

Now we compare the effects of the breakup couplings in the cases of one-proton-halo and one-neutron-halo projectiles. For this purpose, we investigate the $n + ^{7}B$ core-nucleon configuration of $^{8}B$. Since its separation energy is extremely high, this configuration plays no relevant role in the collision dynamics. However, for this comparison we set its separation energy artificially low. We adopt the same value of the $p + ^{7}Be$ configuration, namely 0.137 MeV.

In a different context, Kumar and Bonaccorso [40] used an effective breakup threshold of 0.60 MeV to reduce the difference between the $p + ^{7}Be$ and $n + ^{7}B$ configurations. Their aim was to investigate effects of Coulomb and nuclear breakups in collisions at much higher energies. Their

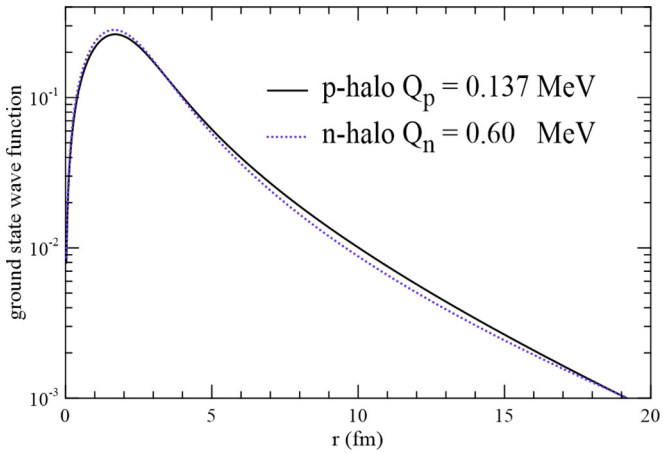


FIG. 9. Ground state wave function of the relative motion of the halo nucleon with respect to the core. The solid and the dotted lines correspond respectively to the $p$-$^7$Be cluster structure with $Q_p = 0.137$ MeV, and to the $n$-$^8$B structure with $Q_n = 0.60$ MeV.

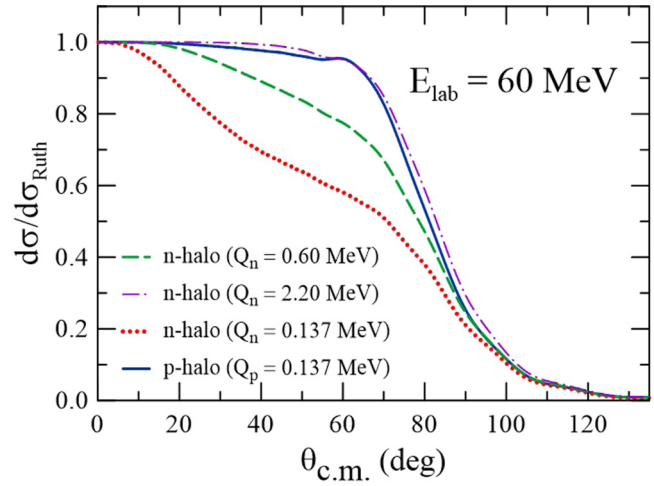


FIG. 10. Comparison of elastic scattering cross sections obtained with CDCC calculations adopting the proton-halo configuration for $^8$B and adopting the neutron-halo configuration with artificially low separation energies. See the text for details.

calculations were performed at $E_{lab} = 576$ MeV, for the same $^{208}$Pb target, where the use of the eikonal approximation is justified. The value of $Q_n = 0.60$ MeV was determined by the condition that the ground state wave function for the $n$-$^7$B motion in $n$-halo configuration be the same as that for the $p$-$^7$Be motion in the $p$-halo configuration. Considering only nuclear breakup, they found that a proton halo behaves exactly as a neutron of higher separation energy.

Even having in mind that we are considereng a very different situation, we performed calculations for the same intermediate value of $Q_n = 0.60$ MeV, to investigate whether the conclusions of Kumar and Bonaccorso are still valid at near-barrier energies, where the eikonal approximation would not be appropriate.

Figure 9 shows the ground srate wave functions for a proton with separation energy $Q_p = 0.137$ MeV (solid line), moving around the $^7$Be core, and for a neutron with separation energy $Q_n = 0.60$ MeV (dotted line), moving around the $^7$B core. As in Ref. [40], one finds very similar wave functions.

We then compare CDCC cross sections for elastic scattering and elastic breakup, adopting the proton-halo ($p + {}^7$Be) and the neutron-halo ($n + {}^7$B) configurations for $^8$B. The elastic scattering cross sections are shown in Fig. 10. The thick solid line is the elastic scattering angular distribution for the $p$-halo configuration, with the experimental separation energy. The curve is the same as in Fig. 4, except for the use of different scales in the $x$ and $y$ axes. The remaining curves are the elastic scattering angular distributions for the $n + {}^7$B cluster structure, with the artificial separation energies $Q_n = 0.137$ MeV (dotted line) and 0.60 MeV (dashed line). Comparing the cross sections for the $p$-halo and $n$-halo structures with the same separation energy (0.137 MeV), we conclude that the effects of the breakup channel are much stronger for the neutron-halo structure. In this case, the ratio to the Rutherford cross section starts deviating from 1 at $\theta \sim 10^o$ and falls continuously as the scattering angle increases. One notices also that the cross section for the $n$-halo structure with $Q_n = 0.60$ MeV is also quite different from that for the p-halo structure with the experimental separation energy. Only for the very large separation energy of 2.2 MeV does one get an elastic cross section for the $n$-halo structure similar to the one for the $p$-halo structure with $Q_p = 0.137$ MeV, as can be observed by the dotted-dashed curve in Fig. 10. In fact, this is not surprising. Despite the similarity of the particle-core ground state wave functions for the two configurations, the matrix elements in the CDCC calculations [Eq. (8)] are not the same. First, the potentials $V(\mathbf{R},\mathbf{r}) = V_{p\text{-T}}(\mathbf{r}_v) + V_{^7\text{Be-T}}(\mathbf{r}_c)$ are different for the $n + {}^7$B and the $p + {}^7$Be halo structures. Second, the bin wave functions, $\phi_{\alpha\neq 0}(\mathbf{r})$ are also different, since for the $n$-halo structure there are no Coulomb phase shifts. These results agree with the conclusions of Ref. [41], were it was shown that different potentials lead to differences in the phase shifts that can significantly affect the breakup cross sections.

Similar calculations were performed for the elastic breakup cross section. The results are shown in Fig. 11. In this case, the

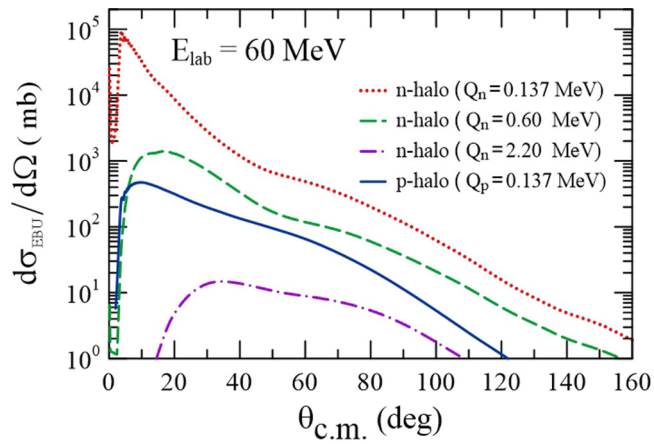


FIG. 11. Similar to Fig. 10 but here the curves represent elastic breakup cross sections.

cross sections for the $n$-halo structure were so much larger that we had to use a logarithmic scale. The notation for the curves are the same as in the previous figure. One notices that the cross sections in the cases of $n$ halo are systematically larger, except in the case of the very high separation energy, $Q_n = 2.20$ MeV. Comparing the results for the two configurations using the same separation energy (0.137 MeV), one finds that the cross section for the $n$ halo is much larger. At forward angles, the difference reaches about two orders of magnitude. This is due to two reasons. First, the Coulomb dipole operator is proportional to the factor $|Z_1A_2 - Z_2A_1|$, where $\{Z_1, A_1\}$ and $\{Z_2, A_2\}$ are respectively the atomic and mass numbers of the core and the nucleon in the configuration. This factor is equal to 3 in the $p$-halo configuration while it is equal to 5 in the $n$-halo configuration. The second factor, which is more important, is that the integrals giving the matrix-element of the bound to continuum couplings are limited by the extension of the halo, which is much larger for an uncharged particle [40].

Comparing the dot-dashed and the solid lines in Fig. 11, one concludes that the elastic breakup cross section for the neutron-halo configuration with $Q_n = 2.20$ MeV is quite different from that for the proton-halo configuration with the experimental separation energy. The former is more than one order of magnitude smaller. This result contrasts with our conclusions about elastic scattering, where the two cross sections were very similar. This is not surprising since the elastic and the breakup amplitudes are very different quantities. The breakup amplitude is given by the matrix element of the coupling interaction, whereas in the elastic amplitude this matrix element is added to that of the optical potential.

We checked also the validity of Kummar and Bonaccorso's conclusions at near-barrier energies in the case of pure nuclear breakup. For this purpose, we performed new calculations neglecting the Coulomb couplings. The results are shown in Fig. 12. Here the solid curve ($p$ halo with $Q_p = 0.137$ MeV) and the dashed curve ($n$ halo with $Q_n = 0.60$ MeV) are quite close. Therefore, we reach the same conclusion as Kumar and Bonaccorso [40] when pure nuclear breakup is considered.

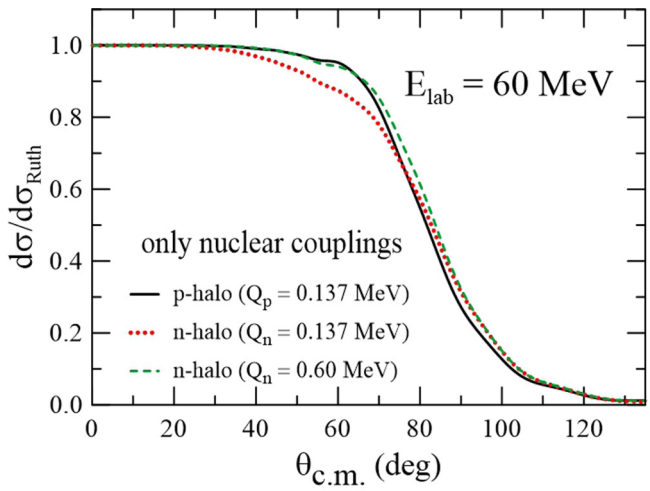


FIG. 12. Same as the previous figure but here the calculations took into account only nuclear couplings, as in the work of Kumar and Bonnacorso [40].

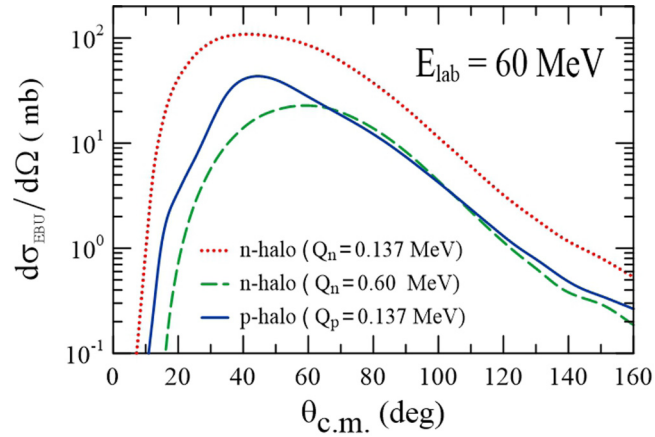


FIG. 13. Similar to Fig. 13 but here the calculations took into account only nuclear couplings.

Figure 13 shows the results of a similar calculation for the elastic breakup cross section. That is, we consider only nuclear couplings. The notation for the three lines is the same as in the previous figure. One can see that the cross section for the neutron-halo configuration with $Q_n = 0.60$ MeV and that for the proton-halo configuration with the experimental separation energy are reasonably close. The agreement of the two calculations is particularly good at large angles.

## V. CONCLUSIONS

We have investigated the effects of the breakup channel in the scattering of $^8$B from $^{208}$Pb at near-barrier energies. These effects are expected to be strong, owing to the low separation energy of the valence proton in $^8$B, which gives rise to a proton halo. The elastic scattering of neutron-halo nuclei has been widely investigated. On the other hand, studies about the scattering of proton-halo nuclei are scarce. There are important differences between the collision dynamics of neutron-halo and proton-halo nuclei. In the former the Coulomb field of the target acts only on the charged core, whereas in the latter the Coulomb field acts also on the valence nucleon.

We have performed several three-body CDCC calculations for elastic scattering and breakup cross sections in the $^8$B -$^{208}$Pb scattering. In our calculations the projectile-target interaction is given by the sum of the potentials between the target and each fragment of the projectile, that is, the core and the valence particle. For the real part of these potentials, we adopted the Akyüz-Winther interaction. For their imaginary parts we used both short-range functions, acting only inside the Coulomb barrier, and functions with a longer range, acting also in the barrier region. We adopted the former in calculations of NCBU and the latter in calculations of elastic scattering and elastic breakup cross sections. In order to achieve good convergence in our calculations, it was necessary to consider multipolarities up to $\lambda = 4$ in the expansion of the interactions.

We described a method to investigate the relative importance of the Coulomb and the nuclear couplings in the collision process, as well as their interference, and this method was applied to the elastic and the breakup cross sections. The results

of the present work for elastic scattering show very clearly that the couplings with the breakup channel suppress the cross sections at forward angles and enhance them at large angles. The Fresnel peak observed at the higher energy $E_{\rm lab} = 170.3$ MeV [24] is no longer present at near-barrier energies. The nuclear couplings enhance the elastic cross sections, whereas the Coulomb couplings suppress them. The suppression found at forward angles can be traced back to the action of the Coulomb forces. Owing to the long range of the dipole coupling, breakup absorption takes place even at distant collisions, which are deflected to small angles. On the other hand, the enhancement at large angles can be attributed to the nuclear couplings, which play an important role in close collisions.

Comparing the cross sections obtained with the full couplings with the ones calculated with pure Coulomb and pure nuclear couplings, we concluded that there is destructive interference in elastic scattering. The same conclusion was reached in the recent work of Diaz-Torres and Moro [6] on elastic scattering of neutron-halo nuclei at near-barrier energies, and also in collisions of $^{8}$B with $^{58}$Ni at near-barrier energies [20,23]. A different situation is found in collisions of halo nuclei at energies well above the barrier. In this case, the couplings with the breakup channel are negligible, and the Fresnel peak can be observed in the elastic scattering data.

We have also investigated the influence of the binding energy of the valence proton on the elastic cross section. For this purpose, we evaluated the cross section using an artificially high value of the separation energy. The resulting cross section did not exhibit the suppression at small angles, showing the usual pattern of heavy ion scattering at near-barrier energies. This is not surprising since the increase of the binding energy eliminates the halo and reduces the intensity of the breakup coupling.

We performed CDCC calculations of breakup cross sections, both elastic and NCBU. We found that the cross sections for the two processes are rather similar. As expected, the Coulomb couplings completely dominate at forward angles and the nuclear couplings are relatively more important at backward angles. We concluded that there is constructive Coulomb-nuclear interference, and that this trend is more pronounced in the case of elastic breakup. The constructive interference in the case of breakup contrasts with the situation encountered in elastic scattering, where the interference is destructive. We remark that there is no inconsistency between these results. The difference stems from the fact that the breakup amplitude is the sum of matrix elements of the Coulomb and of the nuclear couplings, whereas in elastic scattering these matrix elements are summed with the one associated with potential scattering.

We used the method of Thompson *et al.* [36] to evaluate breakup polarization potentials. The most important feature of this potential is its large imaginary part at long distances. This potential was added to the optical potential in a single channel calculation of elastic scattering. The cross section obtained in this way was shown to reproduce accurately the one obtained in the CDCC calculation, which guarantees the validity of this approximate polarization potential.

Finally, we made a comparative study of the effects of the breakup process in collisions of the proton-halo and neutron-halo projectiles. For this purpose, we considered the roles of the $^{7}$Be-$p$ and $^{7}$B-$n$ configurations in the scattering of $^{8}$B projectiles on $^{208}$Pb, adopting artificially low values of the breakup threshold for the $^{7}$B-$n$ configuration. As could be expected, the effects of the breakup channel for neutron-halo are much stronger than in the case of proton-halo projectiles. When the experimental breakup threshold of proton-halo configuration is used for the neutron-halo configuration, the elastic scattering angular distribution is strongly suppressed and the elastic breakup cross section at forward angles increases by two orders of magnitude. However, when only the nuclear breakup is considered, this approach can reasonably describe the elastic scattering and the breakup cross sections, similarly to what was found by Kumar and Bonaccorso [40] at a higher energy.

## ACKNOWLEDGMENTS

This work was partially supported by the CNPq and FAPERJ. We are indebted to Dr. Ian Thompsom for helping us fixing a problem in the calculation of polarization potentials with the FRESCO code.

[1] L. F. Canto, P. R. S. Gomes, R. Donangelo, and M. S. Hussein, Phys. Rep. **424**, 1 (2006).
[2] N. Keeley, R. Raabe, N. Alamanos, and J. L. Sida, Prog. Part. Nucl. Phys. **59**, 579 (2007).
[3] N. Keeley, N. Alamanos, K. W. Kemper, and K. Rusek, Prog. Part. Nucl. Phys. **63**, 396 (2009).
[4] B. B. Back, H. Esbensen, C. L. Jiang, and K. E. Rehm, Rev. Mod. Phys. **86**, 317 (2014).
[5] L. F. Canto, P. R. S. Gomes, R. Donangelo, J. Lubian, and M. S. Hussein, Phys. Rep. **596**, 1 (2015).
[6] A. Diaz-Torres and A. M. Moro, Phys. Lett. B **733**, 89 (2014).
[7] G. R. Satchler and W. G. Love, Phys. Rep. **55**, 183 (1979).
[8] G. R. Satchler, *Direct Nuclear Reactions* (Oxford University Press, Oxford, 1983).
[9] L. F. Canto and M. S. Hussein, *Scattering Theory of Molecules, Atoms and Nuclei* (World Scientific, Singapore, 2013).
[10] C. E. Thorn, M. J. LeVine, J. J. Kolata, C. Flaum, P. D. Bond, and J. C. Sens, Phys. Rev. Lett. **38**, 384 (1977).
[11] A. Di Pietro, V. Scuderi, A. M. Moro, L. Acosta, F. Amorini, M. J. G. Borge, P. Figuera, M. Fisichella, L. M. Fraile, J. Gomez-Camacho *et al.*, Phys. Rev. C **85**, 054607 (2012).
[12] M. Mazzocco, C. Signorini, M. Romoli, A. De Francesco, M. Di Pietro, E. Vardaci, K. Yoshida, R. Yoshida, A. Bonetti, A. De Rosa, T. Glodariu *et al.*, Eur. Phys. J. A **28**, 295 (2006).
[13] V. Morcelle, K. C. C. Pires, M. Rodríguez-Gallardo, R. Lichtenthäler, A. Lépine-Szily, V. Guimarães, P. N. de Faria, D. R. Mendes Junior, A. M. Moro, L. R. Gasques *et al.*, Phys. Lett. B **732**, 228 (2014).

[14] O. R. Kakuee, J. Rahighi, A. M. Sanchez-Benitez, M. V. Andrés, S. Cherubini, T. Davinson, W. Galster, J. Gomez-Camacho, A. M. Laird, M. Lamehi-Rachti *et al.*, Nucl. Phys. A **728**, 339 (2003).
[15] A. M. Sánchez-Benítez, D. Escrig, M. A. G. Álvarez, M. V. Andrés, C. Angulo, M. J. G. Borge, J. Cabrera, S. Cherubini, P. Demarelt, J. M. Espino *et al.*, Nucl. Phys. A **803**, 30 (2008).
[16] L. Acosta, A. M. Sánchez-Benítez, M. E. Gómez, I. Martel, F. Pérez-Bernal, F. Pizarro, J. Rodríguez-Quintero, K. Rusek, M. A. G. Alvarez, M. V. Andrés *et al.*, Phys. Rev. C **84**, 044604 (2011).
[17] L. Standyło, L. Acosta, C. Angulo, R. Berjillos, J. A. Duenas, M. S. Golovkov, N. Keeley, T. Keutgen, I. Martel, M. Mazzocco *et al.*, Phys. Rev. C **87**, 064603 (2013).
[18] M. Cubero, J. P. Fernández-García, M. Rodríguez-Gallardo, L. Acosta, M. Alcorta, M. A. G. Alvarez, M. J. G. Borge, L. Buchmann, C. A. Diget, H. Al Falou *et al.*, Phys. Rev. Lett. **109**, 262701 (2012).
[19] N. Keeley, K. W. Kemper, and K. Rusek, Eur. Phys. J. A **50**, 145 (2014).
[20] J. Lubian, T. Correa, E. F. Aguilera, L. F. Canto, A. Gomez-Camacho, E. M. Quiroz, and P. R. S. Gomes, Phys. Rev. C **79**, 064605 (2009).
[21] J. A. Tostevin, F. M. Nunes, and I. J. Thompson, Phys. Rev. C **63**, 024617 (2001).
[22] J. Lubian, T. Correa, P. R. S. Gomes, and L. F. Canto, Phys. Rev. C **78**, 064615 (2008).
[23] F. M. Nunes and I. J. Thompson, Phys. Rev. C **57**, R2818 (1998).
[24] Y. Y. Yang, J. S. Wang, Q. Wang, D. Pang, J. B. Ma, M. R. Huang, J. L. Han, P. Ma, S. L. Jin, Z. Bai *et al.*, Phys. Rev. C **87**, 044613 (2013).
[25] F. M. Nunes and I. J. Thompson, Phys. Rev. C **59**, 2652 (1999).
[26] J. Lubian and F. M. Nunes, J. Phys. G: Nucl. Part. Phys. **34**, 513 (2007).
[27] I. J. Thompson, Comput. Phys. Rep. **7**, 167 (1988).
[28] A. Barioni, J. C. Zamora, V. Guimarães, B. Paes, J. Lubian, E. F. Aguilera, J. J. Kolata, A. L. Roberts, F. D. Becchetti, A. Villano *et al.*, Phys. Rev. C **84**, 014603 (2011).
[29] M. Kamimura, M. Yahiro, and Y. Iseri, Prog. Theor. Phys. Suppl. **89**, 1 (1986).
[30] N. Austern, Y. Iseri, M. Kamimura, M. Kawai, G. Rawitscher, and M. Yashiro, Phys. Rep. **154**, 125 (1987).
[31] H. Esbensen and G. Bertsch, Nucl. Phys. A **600**, 37 (1996).
[32] R. A. Broglia and A. Winther, *Heavy Ion Reactions* (Westview Press, Boulder, CO, 2004).
[33] L. R. Gasques, L. C. Chamon, P. R. S. Gomes, and J. Lubian, Nucl. Phys. A **764**, 135 (2006).
[34] L. C. Chamon, D. Pereira, M. S. Hussein, M. A. Candido Ribeiro, and D. Galetti, Phys. Rev. Lett. **79**, 5218 (1997).
[35] L. C. Chamon, B. V. Carlson, L. R. Gasques, D. Pereira, C. De Conti, M. A. G. Alvarez, M. S. Hussein, M. A. Cândido Ribeiro, E. S. Rossi, Jr., and C. P. Silva, Phys. Rev. C **66**, 014610 (2002).
[36] I. J. Thompson, M. A. Nagarajan, J. S. Lilley, and M. J. Smithson, Nucl. Phys. A **505**, 84 (1989).
[37] N. Keeley, N. Alamanos, K. Rusek, and K. W. Kemper, Phys. Rev. C **71**, 014611 (2005).
[38] S. Santra, S. Kailas, K. Ramachandran, V. V. Parkar, V. Jha, B. J. Roy, and P. Shukla, Phys. Rev. C **83**, 034616 (2011).
[39] V. V. Parkar, V. Jha, S. K. Pandit, S. Santra, and S. Kailas, Phys. Rev. C **87**, 034602 (2013).
[40] R. Kumar and A. Bonaccorso, Phys. Rev. C **84**, 014613 (2011).
[41] P. Capel and F. M. Nunes, Phys. Rev. C **73**, 014615 (2006).